OPTICS

Revealing non-Hermitian band structure of photonic Floquet media

Jagang Park[1]†‡, Hyukjoon Cho[1]†, Seojoo Lee[1]†, Kyungmin Lee[1], Kanghee Lee[1], Hee Chul Park[2], Jung-Wan Ryu[2], Namkyoo Park[3], Sanggeun Jeon[4], Bumki Min[1]*

Periodically driven systems are ubiquitously found in both classical and quantum regimes. In the field of photonics, these Floquet systems have begun to provide insight into how time periodicity can extend the concept of spatially periodic photonic crystals and metamaterials to the time domain. However, despite the necessity arising from the presence of nonreciprocal coupling between states in a photonic Floquet medium, a unified non-Hermitian band structure description remains elusive. We experimentally reveal the unique Bloch-Floquet and non-Bloch band structures of a photonic Floquet medium emulated in the microwave regime with a one-dimensional array of time-periodically driven resonators. These non-Hermitian band structures are shown to be two measurable distinct subsets of complex eigenfrequency surfaces of the photonic Floquet medium defined in complex momentum space.

INTRODUCTION

Time-periodic driving of a physical system breaks time-reversal and/or time-translational symmetry, thereby enabling observation of exotic new phases of matter in a non- or quasi-equilibrium steady-state setting, such as Floquet quantum Hall states and discrete time crystals (*1*–*3*). As in quantum systems ranging from irradiated Dirac matter to semiconductor quantum wells, a spin chain of trapped atomic ions (*4*) and spin impurities in diamond (*5*), classical systems can offer a route for observing these phases by virtue of mathematical analogy and the correspondence principle. For example, Floquet quantum Hall states, which were first predicted in irradiated graphene and observed in quantum wells and cold atom arrays (*6*–*8*), have been emulated with an array of spatially modulated optical waveguides (*9*–*11*) and acoustic and elastic metamaterials consisting of dynamically modulated resonators (*12*–*14*). Equally important is that an array of driven coupled nonlinear resonators or even a cellular automaton has been recently suggested for observation of discrete time crystalline order in purely classical systems (*15*, *16*).

Sophisticatedly designed photonic platforms have been one of the most prevalent and controllable testbeds for demonstration of exotic wave dynamics (*17*–*25*) and exhibit tremendous potential for imminent realization of time-periodically driven effective media. Wave propagation in periodically driven media can be rationalized based on an effective band analysis in the Floquet picture (*2*). More specifically, for space–time periodic media, the Bloch-Floquet theorem justifies the existence of Floquet sidebands generated by the driving. Therefore, the emergence of such sidebands and their interactions in the effective band description are the key to understanding wave propagation in space–time periodic media (*26*–*33*). In view of this, a new perspective on photonic Floquet media is now being provided by advances in non-Hermitian physics. As was theoretically noted, Maxwell's equations with time-periodic nondispersive permittivity can be recast into an eigenvalue equation with a non-Hermitian Floquet Hamiltonian (*29*). More specifically, the driving-induced interaction between two counter-propagating modes is shown to be nonreciprocal, making the reduced Floquet Hamiltonian unitarily equivalent to a parity-time (PT) symmetric Hamiltonian (*34*, *35*). One of the most notable insights provided by non-Hermitian physics is a completely different way of interpreting a momentum gap in a photonic Floquet medium as a broken PT [or unbroken anti-PT (APT)] phase with a pair of exceptional points being the gap edges along the real momentum axis (*29*, *36*–*38*). Nevertheless, the emergence of driving-dressed quasi-frequency bands of photonic Floquet media, which lie at the heart of understanding these emerging photonic platforms, has not been clearly verified, and thorough experimental scrutinization is yet to come. Here, we take a step further than just experimentally reconstructing the Bloch-Floquet band structure and observing exceptional phase transitions. We show that comprehensive hidden information is embedded in complex eigenfrequency surfaces, the morphology of which can be further revealed by defining and measuring the non-Bloch band structure along a predetermined contour in complex momentum space. These two complementary measurable subsets of complex eigenfrequency surfaces of a photonic Floquet medium could provide a preview of the nonequilibrium dynamics of photonic Floquet media.

RESULTS

Modeling of photonic Floquet media

For emulation of a photonic medium with time-periodic permittivity (Fig. 1A), we consider an effective Floquet medium in the microwave regime, in which a waveguide is loaded with a one-dimensional lattice of coupled time-periodically driven *LC* resonators (Fig. 1B). The necessity of large permittivity modulation leads us to use *LC* resonating unit cells in the construction of the Floquet medium, which, in turn, makes it inherently dispersive. Both the Bloch-Floquet and non-Bloch band structures of this space–time periodic effective medium can be analyzed by setting up a time-varying transmission line (TVTL) model consisting of lumped circuit elements. Specifically, by defining nodal variables of the circuit and corresponding

[1]Department of Mechanical Engineering, Korea Advanced Institute of Science and Technology, Daejeon 34141, Republic of Korea. [2]Center for Theoretical Physics of Complex Systems, Institute for Basic Science, Daejeon 34126, Republic of Korea. [3]Department of Electrical and Computer Engineering, Seoul National University, Seoul 08826, Republic of Korea. [4]School of Electrical Engineering, Korea University, Seoul 02841, Republic of Korea.
*Corresponding author. Email: bmin@kaist.ac.kr
†These authors contributed equally to this work.
‡Present address: Department of Electrical Engineering and Computer Sciences, University of California, Berkeley, Berkeley, CA 94720, USA.

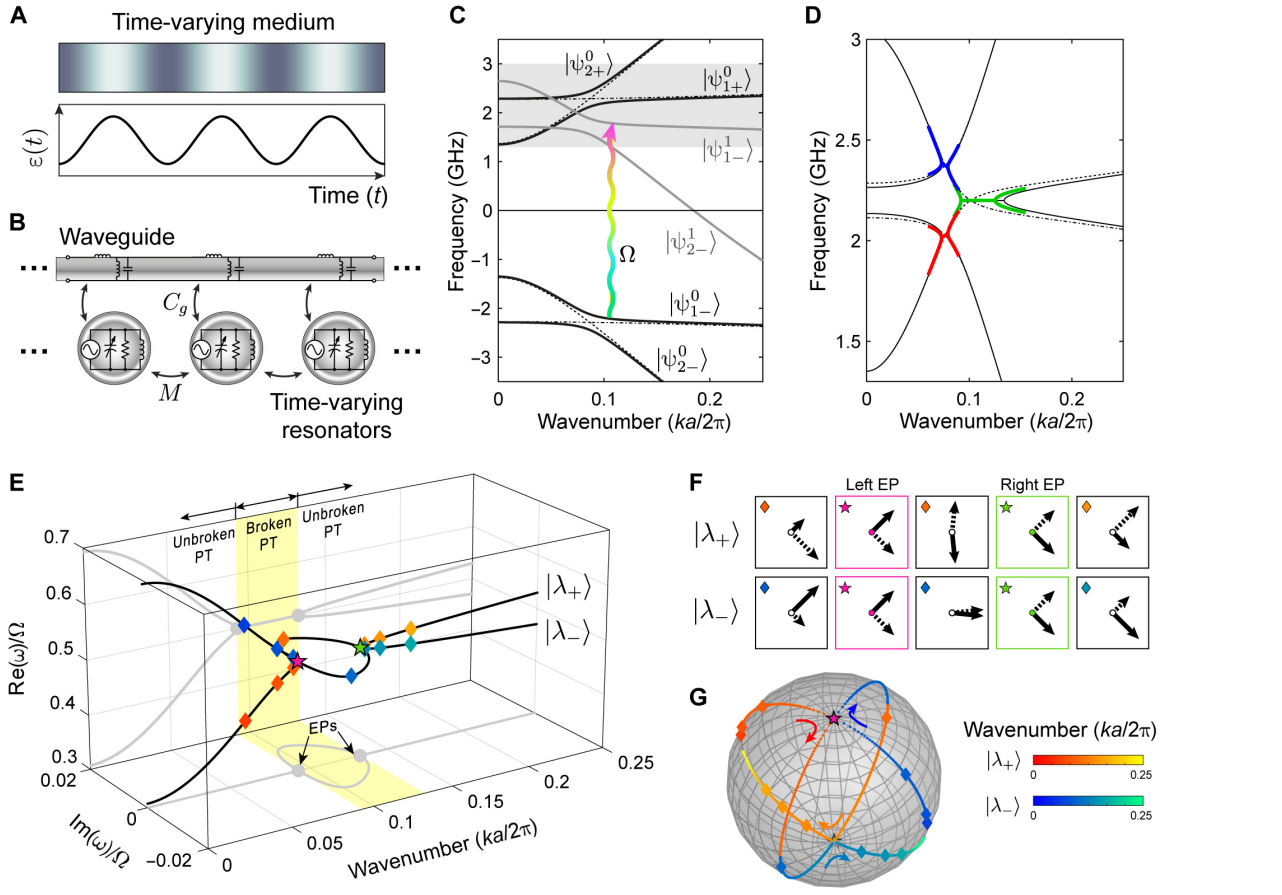

Fig. 1. Bloch-Floquet band structures and exceptional transitions. (**A**) Homogeneous Floquet medium with time-periodic permittivity. (**B**) Schematic illustration of a one-dimensional effective photonic Floquet medium consisting of spatially concatenated time-varying *LC* resonators and a waveguide. The resonator capacitance and, correspondingly, the resonance frequency are assumed to be time periodically modulated. Each of the resonators is capacitively coupled to the waveguide and inductively coupled to its nearest-neighbor resonators. (**C**) Static band structure (drawn with black lines) of the undriven medium and creation of sidebands (drawn with gray lines) of negatively signed frequency in the photonic Floquet medium. The resonator and waveguide bands are drawn with dashed-dotted and dashed lines, respectively. (**D**) Formation of the primary (drawn with green lines) and secondary (drawn with blue and red lines) momentum gaps dressed by the driving-induced interaction between static bands and sidebands. Dashed lines are calculated without considering the interactions. (**E**) Complex eigenfrequencies plotted as a function of the real wave number in the proximity of the primary momentum gap. Mode coalescence behavior and exceptional transitions are observed at the edges of the primary momentum gap. The momentum gap is associated with the PT broken region. (**F**) Bloch sphere representation of eigenmodes $|\lambda_{\pm}\rangle$ at various wave numbers denoted by scatters in (E). (**G**) The mode coalescence and bifurcation occur at the north and south poles of the Bloch sphere.

modal amplitudes, a Floquet Hamiltonian in momentum space can be derived, from which the exceptional phase transition can be systematically investigated (see the Supplementary Materials). For an undriven medium, the hybridization between a waveguide and a resonator mode results in two static Bloch bands $|\psi^0_{1+}\rangle$ and $|\psi^0_{2+}\rangle$, drawn with solid black lines in Fig. 1C (also drawn are two mirror symmetric negative frequency bands $|\psi^0_{1-}\rangle$ and $|\psi^0_{2-}\rangle$, with a line of symmetry being the momentum or wave number axis). In the preceding clarification, the static Bloch bands are labeled by $|\psi^0_{m\pm}\rangle$, where m denotes the lower (m= 1) or higher (m= 2) Bloch bands, with the following sign representing either a positive (+) or a negative (−) frequency. As a side note, the validity of the transmission line model is most clearly confirmed by its comparison with the static band structure obtained from full numerical simulations (see fig. S1).

Bloch-Floquet band structures and exceptional phase transitions

When the time-periodic modulation is turned on, Fourier sidebands can exist in the medium; for instance, two such sidebands, $|\psi^1_{1-}\rangle$ and $|\psi^1_{2-}\rangle$, are indicated by solid gray lines in Fig. 1C (where the superscript in the band labeling denotes the harmonic order of the driving involved in the formation of the sidebands). As a result, the static states can now be coupled to the sidebands at the band crossing points by a parametric nonreciprocal interaction. In this Bloch-Floquet framework, horizontal momentum gaps are opened because of the nonreciprocal coupling between the static band and the driving-generated sideband of negative frequency (Fig. 1D). For example, the opening of a primary momentum gap (appearing at half the driving frequency, i.e., Ω/2) is attributed to the nonreciprocal coupling and associated hybridization between $|\psi^0_{1+}\rangle$ and $|\psi^1_{1-}\rangle$. Two secondary momentum gaps are symmetrically located along the frequency axis with respect to the primary momentum gap frequency; the upper secondary gap is opened by the hybridization between $|\psi^0_{2+}\rangle$ and $|\psi^1_{1-}\rangle$, while the lower secondary gap is opened by the hybridization between $|\psi^0_{1+}\rangle$ and $|\psi^1_{2-}\rangle$.

The aforementioned qualitative description is clearly captured by considering the following 2 × 2 reduced effective Floquet Hamiltonian

matrix that describes the interaction between the static band and the sideband (see the Supplementary Materials)

$$H^F_{\mathrm{red}}(k)=\begin{bmatrix}\omega_{\mu-}(k)+\Omega & \kappa^F_{\mu\nu}(k)\\ -\kappa^{F*}_{\nu\mu}(k) & \omega_{\nu+}(k)\end{bmatrix}$$

where $\omega_{\mu-(\nu+)}$ is the modal frequency of the μth (νth) negative (positive) frequency band, Ω is the driving frequency, and $\kappa^F_{\mu\nu}$ is the driving-induced coefficient of coupling between the μth negative and νth positive frequency bands. In particular, for the interaction between two oppositely signed lower bands $|\psi^0_{1+}\rangle$ and $|\psi^1_{1-}\rangle$, the reduced Floquet Hamiltonian can be decomposed into the sum of an APT symmetric matrix and a scalar multiple of the identity matrix

$$H^F_{\mathrm{red}}(k)=\frac{\Omega}{2}\mathbf{I}_2+\begin{bmatrix}-\left(\omega_{1+}(k)-\frac{\Omega}{2}\right)^* & \kappa^F_{11}(k)\\ -\kappa^{F*}_{11}(k) & \omega_{1+}(k)-\frac{\Omega}{2}\end{bmatrix}=\frac{\Omega}{2}\mathbf{I}_2+H^F_{\mathrm{APT}}(k)$$

Here, the dissipative loss of the resonators was included in the analysis through the use of the Rayleigh dissipation function, which makes the band frequencies $\omega_{\mu-(\nu+)}$ intrinsically complex valued. We can also show that the APT symmetry of the reduced Floquet Hamiltonian matrix is preserved regardless of the inclusion of dissipative loss. Straightforwardly, the eigenvalues of the reduced Floquet Hamiltonian matrix (i.e., eigenfrequencies of dressed bands) are found to be

$$\lambda_{\pm}(k)=\frac{\Omega}{2}+j\mathrm{Im}(\omega_{1+})\pm\sqrt{\left(\mathrm{Re}(\omega_{1+})-\frac{\Omega}{2}\right)^2-\mathrm{Im}(\omega_{1+})^2-|\kappa^F_{11}(k)|^2}$$

The eigenfrequency plotted as a function of the real wave number signifies two distinct phases of the photonic Floquet medium (Fig. 1E). In the region of real wave numbers satisfying $|\mathrm{Re}(\omega_{1+})-\Omega/2|<\sqrt{|\mathrm{Im}(\omega_{1+})|^2+|\kappa^F_{11}|^2}$, the two complex eigenfrequencies become conjugate to each other (a broken PT or an unbroken APT phase), while the eigenvalues become distinctive

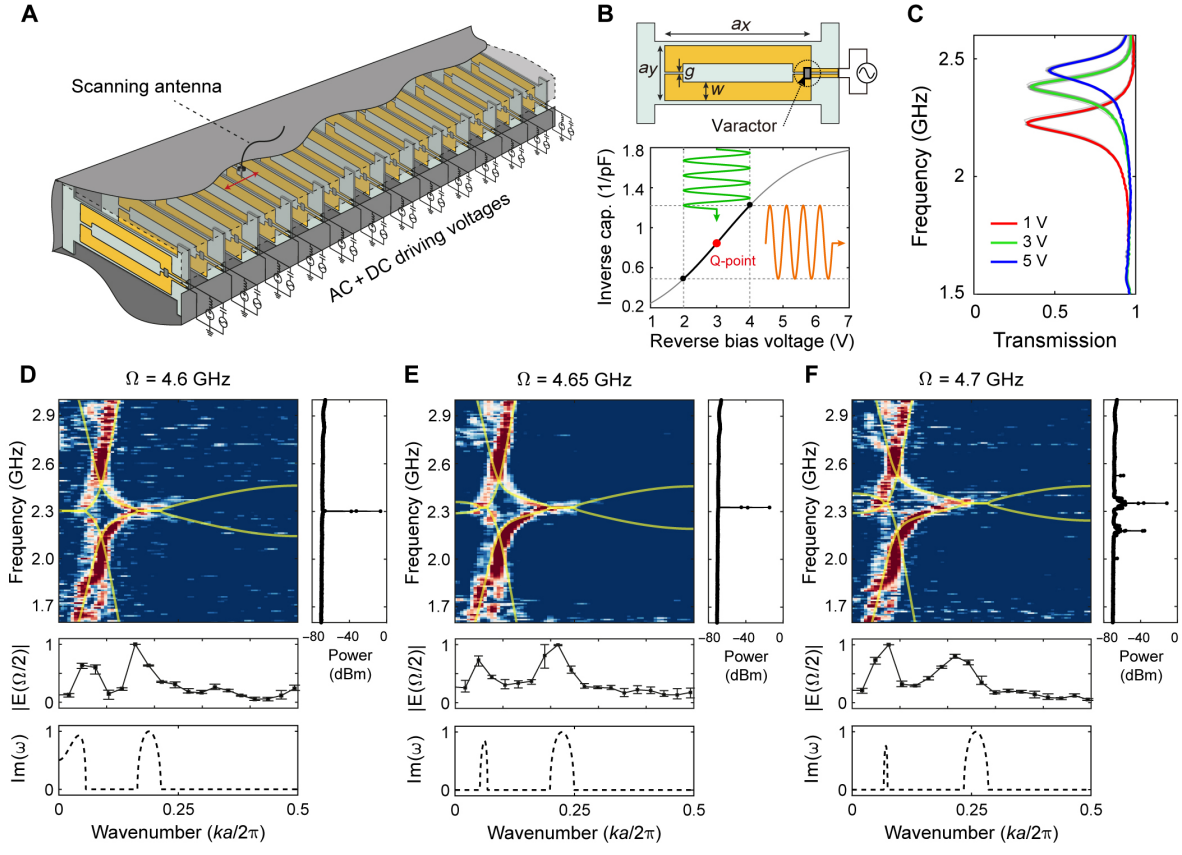

Fig. 2. Experimental reconstruction of the Bloch-Floquet band structure. (**A**) Schematic illustration of the microwave Floquet medium comprising an array of driven *LC* resonators in a rectangular waveguide. (**B**) Geometry of a split-ring *LC* resonator patterned by a printed circuit board manufacturing process on a low-loss dielectric substrate. A varactor diode is soldered to the capacitive gap of the resonator. The geometrical parameters of the unit cell are designed as follows: $a_x = 80$ mm, $a_y = 30$ mm, $w = 10$ mm, and $g = 1$ mm. The spacing between the unit cells is set to 10 mm. Below is the plot of the inverse capacitance as a function of reverse bias voltage applied to the varactor diode (SMV1247, Skyworks). In the measurements, the Q-point was set by maximizing the signal parametrically oscillating at the primary momentum gap frequency. The orange line represents the variation in the inverse capacitance for the sinusoidal driving voltage excitation drawn with a green line. (**C**) Averaged transmission spectra of the unit cells for bias voltages of 1, 3, and 5 V. Gray lines show individually measured transmission spectra of 24 different unit cells. (**D** to **F**) Two-dimensional Fourier transformed electric fields for modulation frequencies of (D) 4.6, (E) 4.65, and (F) 4.7 GHz. Theoretically calculated band structures are overlaid on the measured results with semitransparent violet lines. Middle panels are the horizontal cut of the transformed field along the real momentum axis at the primary momentum gap frequency. Bottom panels are the imaginary part of the eigenfrequency plotted as a function of wave number. The power spectral density of the radiation from the strongly driven Floquet medium is shown in the right panel. Sharp oscillating peaks are observed at momentum gap frequencies.

real outside the region (an unbroken PT or a broken APT phase). Accordingly, exceptional phase transitions are explicitly revealed at the two edges of a momentum (or wave number) gap, where two mode coalescing singularities along the real momentum axis separate the broken PT region (inside the momentum gap) from two unbroken PT regions (outside the momentum gap). This mode coalescence behavior of two eigenstates can also be visualized in the Bloch sphere representation (see Fig. 1F). With an increase in the momentum, the eigenstates coalesce and bifurcate at the lower momentum gap edge (corresponding to the south pole in the Bloch sphere), and they coalesce and bifurcate once more at the higher momentum gap edge (i.e., the north pole in the Bloch sphere). Notably, a non-Hermitian Hamiltonian matrix with nonreciprocal and/or dissipative coupling terms in its off-diagonal elements can be unitarily transformed into the matrix with gain and loss terms in its diagonal elements.

Experimental verification of Bloch-Floquet band structures

For experimental verification of Bloch-Floquet band structures and exceptional phase transitions, we constructed an effective Floquet medium designed to operate at microwave frequencies by concatenating split-ring resonators inside a customized rectangular waveguide (Fig. 2A). Each resonator is embedded with a DC-biased varactor diode in the capacitive gap; through the application of an AC voltage to the diode terminals, direct modulation of the total capacitance and, correspondingly, the resonance frequency can be achieved (Fig. 2, B and C). Here, the driving strength δ_0 is defined as the modulation depth of the inverse resonator capacitance (see the Supplementary Materials). As the first step in verifying the theoretical prediction, Bloch-Floquet band structures were experimentally reconstructed by mapping the spatiotemporal field evolution within the photonic Floquet medium. More specifically, we recorded the temporal evolution of the electric field radiated by a source antenna with a probe antenna scanning over the Floquet medium (see the Supplementary Materials). Then, a two-dimensional Fourier transform of the measured electric field was used to reconstruct the Bloch-Floquet band structure. Here, note that the Floquet medium under test was finite sized along the propagation direction; for the first part, the number of unit cells (N) was set to 36 to ensure reasonable resolution along the momentum axis while keeping the external driving under optimal conditions. To test the validity of the experimental methodology, we first confirmed the emergence of driving-generated sidebands $|\psi^1_{1+}\rangle$ and $|\psi^1_{2+}\rangle$ from the positive frequency lower bands (see fig. S2 for the case of driving at 0.6 GHz).

The driving-generated sidebands of a negative frequency state, which is of even greater interest, can be resolved, in principle, once the driving frequency exceeds approximately twice the lower band cutoff, i.e., $\Omega \gtrsim 2\Omega_{c1}$. In Fig. 2 (D to F), these sidebands of negative frequency and resulting dressed bands are visualized in the reconstructed Bloch-Floquet band structure, on which theoretically calculated bands are overlaid (the real eigenfrequencies are drawn with semitransparent violet lines). The opening of momentum gaps can be confirmed by clarifying the locations of high transformed field intensities in the reconstructed Bloch-Floquet band structure, which can be attributed in part to the existence of a temporally growing mode of complex-valued eigenfrequency with a positive imaginary part (see Fig. 1E). This observation can be made clearer by plotting the transformed field intensity as a function of the momentum at half the driving frequency (Fig. 2, D to F, middle) and comparing it with the calculated imaginary part of the eigenfrequency. According to the comparison, the peak field intensity position on the momentum axis, at which the maximal net gain is expected, is in good agreement with the analysis (Fig. 2, D to F, bottom). The theoretical prediction is also supported by measured standing wave–like mode field patterns near the two edges of the primary momentum gap (see fig. S3). Specifically, the temporal phase shift of ~$\pi/2$ in between is analogous to the spatial phase shift of $\pi/2$ between the (energy) band edge modes of a spatially periodic photonic structure.

Here, several more remarks can be made on the momentum gaps in the Bloch-Floquet band structure. First, the primary momentum gap widens as half the driving frequency approaches the frequency of the band edge from the lower side (under the condition of constant driving strength). This is in part due to the modal energy being confined more in the resonators than in the waveguide near the band edges. Second, the midgap location of the primary momentum gap, i.e., the midpoint (in wave number) between the left and right edges of a horizontal momentum gap, lies approximately on the static Bloch band $|\psi^0_{1+}\rangle$. This is attributed to the fact that the primary momentum gap starts to open at the intersection of $|\psi^0_{1+}\rangle$ and $|\psi^1_{1-}\rangle$ with an increase in driving strength. This observation can also be confirmed by calculating the midgap location as a function of the driving frequency and comparing it with the measured data (Fig. 3A). Last, the intensity peak at a lower wave number ($ka/2\pi \sim 0.06$) observed for a higher driving frequency (Fig. 2, D to F, middle and bottom) is indicative of opening of a tertiary gap at the primary gap frequency. This tertiary gap originates from the hybridization between $|\psi^0_{2+}\rangle$ and $|\psi^1_{2-}\rangle$ and can be observed for a driving frequency higher than approximately twice the higher band cutoff ($\Omega \gtrsim 2\Omega_{c2}$).

Another compelling argument in support of opening of momentum gaps and occurrence of exceptional transitions is provided by the spectral measurement of noise-initiated in-gap mode parametric oscillation. In these experiments, in contrast to the Bloch-Floquet band structure reconstruction measurements, the power spectral

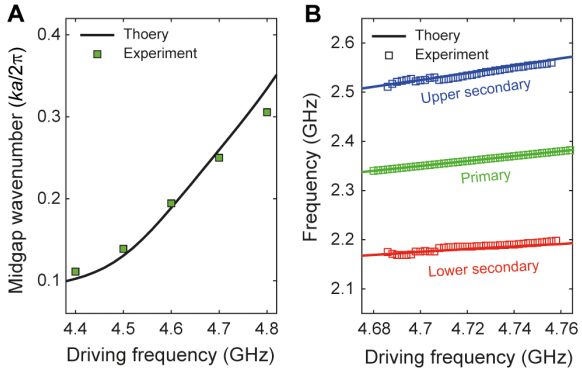

Fig. 3. Identification of momentum gap locations in the Bloch-Floquet band structure. (**A**) Plot of midgap wave numbers as a function of the driving frequency (for the primary momentum gap). Theoretically calculated midgap wave numbers at which the imaginary part of the complex eigenfrequency becomes maximized are drawn with a black line. Experimentally measured midgap wave numbers are estimated from the locations of Fourier transformed intensity maxima at the primary momentum gap frequencies. (**B**) Plot of momentum gap frequencies as a function of the driving frequency. Primary and secondary momentum gap frequencies are estimated from the experimentally measured parametric oscillation frequencies (see Fig. 2, D to F) and compared with the theoretical predictions from the TVTL model (drawn with lines). Parametric oscillations are attributed to the loss-compensated unstable modes inside the primary (green) and secondary (top; blue, bottom; red) momentum gaps.

density of the field radiated from the Floquet medium was recorded without any source signal being provided. When the driving strength is increased up to the point where the total loss of the Floquet medium is compensated by the parametric gain within the gap, a noise-initiated oscillating behavior is induced (see fig. S4). Then, the precise frequency of the primary gap and the approximate frequencies of secondary gaps at which the net gain is maximized can be identified by the spectral positions of the parametrically oscillating peaks (see Fig. 2, D to F, vertical panels). As predicted, secondary momentum gaps are observed near the spectral positions where $|\psi^0_{2+}\rangle$ and $|\psi^1_{1-}\rangle$, or $|\psi^0_{1+}\rangle$ and $|\psi^1_{2-}\rangle$, are presumed to cross in the absence of coupling ($\omega_{1-} + \Omega = \omega_{2+}$, or $\omega_{2-} + \Omega = \omega_{1+}$) (*28*, *31*). By tracking the oscillation frequencies with the variation in the driving frequency (Fig. 3B), we confirmed that the secondary momentum gaps are always symmetrically positioned along the frequency axis with respect to the primary gap, as predicted by theory.

Complex eigenfrequency surfaces and non-Bloch band structures

In the aforementioned discussions, all the observed and measured phenomena are interpreted on the basis of the relationship between complex energy and real momentum. Now, we will investigate the characteristics of photonic Floquet media within the non-Bloch framework. For this purpose, we measured the phase retardation of a wave of various frequencies passing through a finite-sized Floquet medium ($N = 24$) (*39*). Here, note that this measurement scheme is valid only when the driving strength δ_0 is maintained relatively low; this condition ensures that parametric gain-enhanced multiple reflection can be assumed to be minimal (see fig. S5). Within the driving strength regime where the single-pass approximation is valid, a real-valued modal wave number can be assigned to the wave of a given (real-valued) frequency as $k_r = \Delta\phi/(Nd)$, where $\Delta\phi$ is the measured phase retardation and d is the thickness of the unit cell. The non-Bloch band structure probed by this measurement protocol enables us to reveal the morphology of complex eigenfrequency surfaces of the Floquet medium in complex momentum space. Notably, the complex eigenfrequency surfaces also contain the Bloch-Floquet band structure as a subset, i.e., the intersections of the surfaces with the plane defined by $\mathrm{Im}(k) = 0$. Therefore, knowledge of both band structures can provide a more in-depth understanding of the photonic Floquet medium. To illustrate this, theoretically calculated real and imaginary eigenfrequency surfaces are plotted in complex momentum space for three different values of the driving strength (Fig. 4, A to F). As observed in the plots, the real (or

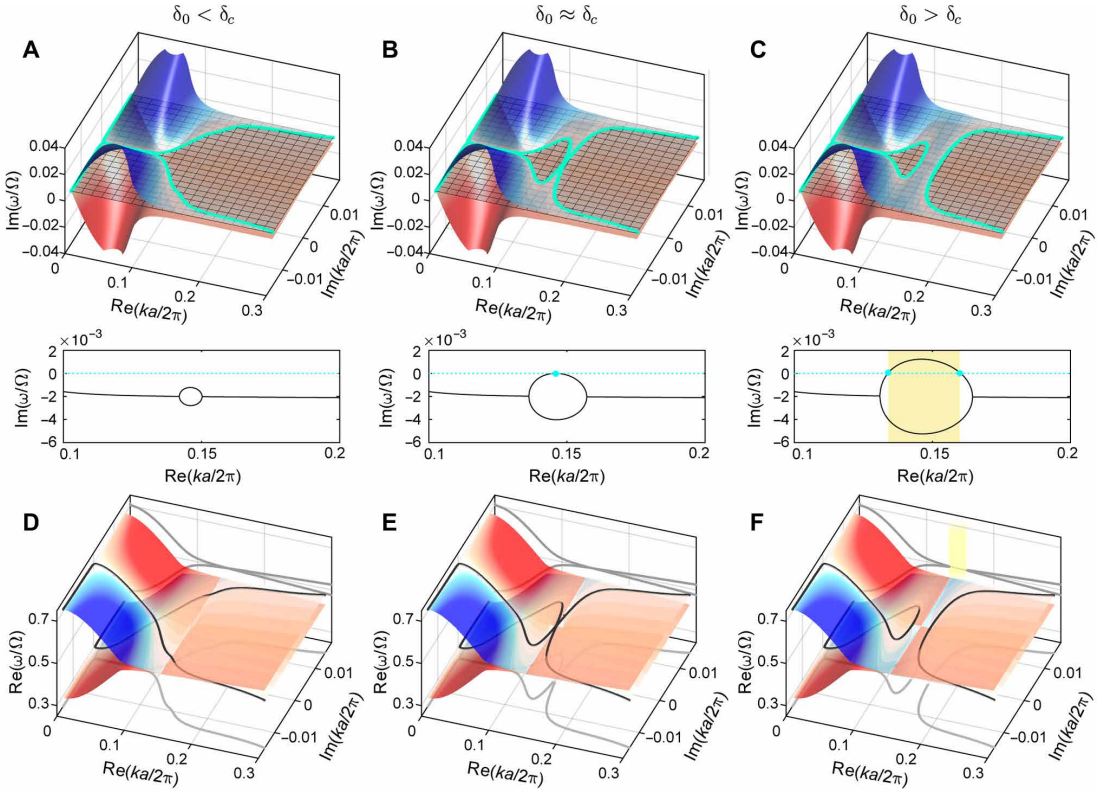

Fig. 4. Complex eigenfrequency surfaces and non-Bloch band structures. (**A** to **C**) Imaginary eigenfrequency surfaces plotted in complex momentum space for three distinct values of the driving strength, i.e., weak driving ($\delta_0 < \delta_c$), critical driving ($\delta_0 = \delta_c$), and strong driving ($\delta_0 > \delta_c$). The imaginary eigenfrequency surfaces consisting of a pair of curved sheets are color-coded by the values of their imaginary part. The zero imaginary eigenfrequency contours are drawn with cyan-colored lines. Bottom panels show the enlarged view of the imaginary frequency bifurcation (solid black lines) on the surface of $\mathrm{Im}(k) = 0$, and the dotted cyan lines are located at $\mathrm{Im}(\omega) = 0$. (**D** to **F**) Real eigenfrequency surfaces plotted in complex momentum space for three distinct values of the driving strength, i.e., weak driving ($\delta_0 < \delta_c$), critical driving ($\delta_0 = \delta_c$), and strong driving ($\delta_0 > \delta_c$). The real eigenfrequency surfaces consisting of a pair of curved sheets are color-coded by the values of their corresponding imaginary eigenfrequency. Here, the black lines (drawn on the surface) are the real eigenfrequencies corresponding to the complex momenta on cyan-colored contours (i.e., zero imaginary eigenfrequency contours). Shown on the sidewall are the non-Bloch band structures that can be obtained from phase retardation measurements (see Fig. 5). Note that phase discontinuity is observed only for strong driving (highlighted by a yellow-colored area).

imaginary) eigenfrequency surface is composed of a pair of curved sheets, the characteristics of which are signified by two exceptional points in complex momentum space (see fig. S6). In Fig. 4 (A to F), we can observe that a driving-induced surface morphological change is more pronounced in the region of complex momenta with real values approximately falling in the momentum gap. In contrast, a change in the resonator dissipation rate (see the resistors in Fig. 1B) leads to preferential bending and leveling of the surfaces near the band edge (see figs. S6 and S7 for an expanded view of driving- and dissipation-induced changes in the complex eigenfrequency surfaces).

These results prove that the performed phase retardation measurement can be thought of as a selection process that samples only a subset of the real eigenfrequency surfaces in a designated way. The selection rule imposes the condition that the imaginary eigenfrequency must be zero, i.e., Im(ω) = 0, which can be justified based on the observed steady-state behavior of the photonic Floquet medium. This steady-state condition enables us to define contours in complex momentum space (as denoted by cyan-colored contours in Fig. 4, A to C) and to construct the non-Bloch band structure from the real eigenfrequencies evaluated along these contours (see black lines on the real eigenfrequency surface and their projection onto the sidewalls in Fig. 4, D to F). For the case of weak driving ($\delta_0 < \delta_c$), the imaginary part of the eigenfrequency bifurcates within the momentum gap, but the sign is still negative due to dissipation-induced lowering of the eigenfrequency surfaces (see Fig. 4A). Then, the selection rule guarantees phase continuity along the real momentum axis at half the driving frequency (Fig. 4D). In contrast, for the case of strong driving ($\delta_0 > \delta_c$), the sign of a larger bifurcated imaginary eigenfrequency becomes positive near the real momentum axis, changing the zero imaginary eigenfrequency contours such that a phase discontinuity occurs along the real momentum axis at half the driving frequency (see Fig. 4, C and F). These two driving regimes are differentiated at a critical driving strength ($\delta_0 = \delta_c$), where the larger of bifurcated imaginary eigenfrequencies becomes zero (Fig. 4, B and E).

Complex Brillouin zone

The difference between non-Bloch and Bloch-Floquet band structures can be clearly noted by plotting the corresponding Bloch phase factors $\beta \equiv \exp(jk)$ for two subsets of complex momentum defined by Im(ω) = 0 and Im(k) = 0. The latter condition ensures that the Bloch phase factor $\beta_{\mathrm{Im}(k)=0}$ takes continuous values on a unit circle centered at the origin of the Gauss plane (drawn with black dashed lines in Fig. 5, A to C), which represents the conventional Brillouin zone for the Bloch-Floquet band structure. In contrast, the Bloch phase factor $\beta_{\mathrm{Im}(\omega)=0}$ does not trace the unit circle (drawn with cyan lines in Fig. 5, A to C), the consequences of which are reflected in the non-Bloch band structure measured in the steady state. More specifically, for the case of strong driving ($\delta_0 > \delta_c$), the trace of $\beta_{\mathrm{Im}(\omega)=0}$ no longer encircles the origin but exhibits gaps in the angular direction (highlighted by yellow sectors in Fig. 5C). The angular gaps in the trace imply that there exists a finite range of Re(k) for which real-valued eigenfrequencies are absent. Therefore, the non-Bloch band structure projected onto the Re(k)-Re(ω) plane exhibits a discontinuous jump along the real momentum axis at the primary momentum gap frequency. This is in stark contrast to the immediate opening of momentum gaps in the Bloch-Floquet band structure, which is observed regardless of the driving strength (see Fig. 4, D to I).

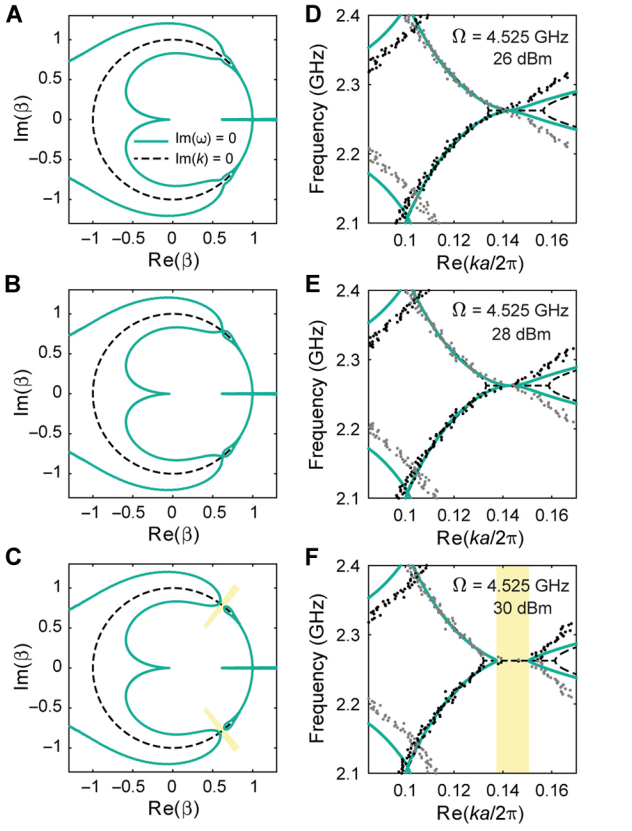

Fig. 5. Comparison between non-Bloch and Bloch-Floquet band structures. (**A** to **C**) Traces of the Bloch phase factor $\beta = \exp(jk)$ plotted on the complex plane for two different subsets of complex momentum. One is based on the conventional definition of the Brillouin zone (denoted by a dashed black unit circle; $|\beta| = 1$), and the other is based on the extended Brillouin zone from steady-state phase retardation measurements [drawn with a cyan solid line; Im(ω) = 0]. Here, the complex Brillouin zone is introduced for interpretation of measured phase retardation data. For strong driving, angular gaps in the traces of the Bloch phase factor are highlighted with yellow sectors. (**D** to **F**) Theoretically calculated Bloch-Floquet band structure defined on the real momentum axis (denoted by dashed black lines) and non-Bloch band structures (denoted by cyan solid lines). The non-Bloch band structures are reconstructed from the phase retardation measurements at three different values of the driving strength approximately corresponding to (D) weak, (E) critical, and (F) strong driving (with the power being measured before splitting the driving signal). The black dots represent the measured data, while the gray dots are the mirror-reflected ones with a line of symmetry being the momentum gap frequency ω = Ω/2. The yellow region in (F) is associated with the angular gaps shown in (C).

As shown in the reconstructed non-Bloch band structures (Fig. 5, D to F), an abrupt phase jump is observable only when the driving strength becomes larger than the critical value, which is in a good agreement with the theoretical prediction. As demonstrated, the non-Bloch band structure reconstruction, when combined with variations in parameters (e.g., driving strength or the rate of dissipation), can provide sectional information on the morphology of complex eigenfrequency surfaces in complex momentum space, which calls for a further in-depth investigation on how the non-Hermiticity of photonic Floquet media manifests itself in complex momentum space (*40*–*42*).

DISCUSSION

Although one of the most intriguing features of a photonic Floquet medium is the creation of sidebands of negative frequency and their interactions leading to exceptional phase transitions, the interpretation of experimental observations given here is based on a linearized model. In the strong driving regime, however, ignoring nonlinearity along with dissipation and fluctuation becomes increasingly difficult. This implies that a thorough understanding of these effects is required for characterization of exotic new phases in nonequilibrium photonic matter. In this regard, nonreciprocal phase transitions in active matter seem to share many features in common with the proposed nonequilibrium photonic Floquet medium, which coherently exchanges energy with its environment (*16*, *43*, *44*). In particular, classical many-body effects can be manifested by nonlinearity; whether a subharmonic spectral component arising at the momentum gap is associated with many-body time crystalline behavior would be an especially interesting question for which further investigation is highly demanded. Considered from another perspective, the proposed platform is reminiscent of classical coherent Ising machines constructed by coupling nonlinear oscillators for solving computationally hard problems (*45*). The complex band structure analysis also provides a new perspective on designing driven nonlinear photonic devices such as parametric amplifiers, oscillators, and isolators. Last, photonic Floquet media are an effective spatiotemporal matter platform generalized from conventional spatially periodic structures and are poised to create a new area of research in non-Hermitian photonics.

MATERIALS AND METHODS

Transmission line modeling of static band structures

We established a TVTL model with lumped circuit elements to analyze Floquet media, the properties of which are simultaneously dispersive and time varying. The static band structure can be obtained simply by assuming that none of the constituting circuit elements of the TVTL are time varying. The model consists of a chain of driven *LC* resonators and a bus waveguide, as depicted in Fig. 1B. The constituting resonators are assumed to be capacitively coupled to the waveguide and inductively coupled to their nearest neighbors. The Lagrangian can be given as a function of accumulated charge and electric current (Q and $\dot{Q}$) at every nodal point and circuit element of the TVTL

$$\mathcal{L} = \sum_n \left(\frac{1}{2} L_0 |\dot{Q}_n^{L_0}|^2 + \frac{1}{2} L_s |\dot{Q}_n^{L_s}|^2 + \frac{1}{2} L_r |\dot{Q}_n^{L_r}|^2 + \sum_i M_i \dot{Q}_n^{L_r} \dot{Q}_{n+i}^{L_r} - \frac{|Q_n^a|^2}{2C_0} - \frac{|Q_n^b|^2}{2C_r} - \frac{Q_n^a Q_n^b}{C_g} \right)$$

where L_0, L_s, C_0, L_r, C_r, M_i, and C_g are the series inductance, shunt inductance and shunt capacitance of the bus waveguide, inductance and capacitance of the resonator, mutual inductance between ith nearest-neighbor resonators, and coupling capacitance between the resonator and the bus waveguide. The superscripts on $\dot{Q}$s indicate the circuit elements conducting the electric current, while the superscripts a and b on Qs denote the waveguide and resonator nodes, respectively. The Legendre transformation of the Fourier transformed Lagrangian gives the Hamiltonian in momentum space as a function of charge and node flux (Q and Φ), which are the canonical variables for electric circuits. By defining modal amplitudes of the waveguide (a_κ) and the coupled resonators (b_κ) as linear combinations of these canonical variables, the Hamiltonian can be written as

$$H_\kappa = \Omega_\kappa (a_\kappa^\dagger a_\kappa + a_{-\kappa}^\dagger a_{-\kappa})/2 + \omega_\kappa (b_\kappa^\dagger b_\kappa + b_{-\kappa}^\dagger b_{-\kappa})/2 - g_\kappa [(a_\kappa^\dagger + a_{-\kappa})(b_\kappa + b_{-\kappa}^\dagger) + (b_\kappa^\dagger + b_{-\kappa})(a_\kappa + a_{-\kappa}^\dagger)]/2$$

where Ω_κ and ω_κ are the frequencies of the bus waveguide and the coupled resonator with momentum κ, respectively, and g_κ is the coefficient of coupling between these two modes, which are found as follows:

$$\Omega_\kappa = \sqrt{1/L_s C_0 + [4\sin^2(\pi/N)\kappa]/L_0 C_0}$$

$$\omega_\kappa = 1/\sqrt{[L_r + \Sigma_i M_i \cos(2\pi/N)\kappa i] C_r}$$

$$g_\kappa = \sqrt{C_0 C_r \Omega_\kappa \omega_\kappa}/2C_g$$

On the basis of mode amplitudes $(a_\kappa, b_\kappa, a_{-\kappa}^\dagger, b_\kappa^\dagger)$, the effective Hamiltonian is found in the form of a matrix as

$$\widetilde{H}_\kappa = \frac{1}{2} \begin{bmatrix} \Omega_\kappa & -g_\kappa & 0 & -g_\kappa \\ -g_\kappa & \omega_\kappa & -g_\kappa & 0 \\ 0 & g_\kappa & -\Omega_\kappa & g_\kappa \\ g_\kappa & 0 & g_\kappa & -\omega_\kappa \end{bmatrix}$$

Then, by calculating eigenvalues of $\widetilde{H}_\kappa$, the exact static band structure of the model can be found to be

$$\omega_1^2 = \frac{1}{2}\left[(\Omega_\kappa^2 + \omega_\kappa^2) - \sqrt{(\Omega_\kappa^2 - \omega_\kappa^2)^2 + 16\Omega_\kappa \omega_\kappa g_\kappa^2} \right]$$

$$\omega_2^2 = \frac{1}{2}\left[(\Omega_\kappa^2 + \omega_\kappa^2) + \sqrt{(\Omega_\kappa^2 - \omega_\kappa^2)^2 + 16\Omega_\kappa \omega_\kappa g_\kappa^2} \right]$$

For the sake of simplicity, an approximated Hamiltonian can be obtained by applying the rotating-wave approximation

$$H_\kappa = \Omega_\kappa a_\kappa^\dagger a_\kappa + \omega_\kappa b_\kappa^\dagger b_\kappa - g_\kappa (b_\kappa^\dagger a_\kappa + a_\kappa^\dagger b_\kappa)$$

which can be used to derive approximate static band structures of the transmission line model

$$\omega_{1\pm} = \pm\frac{1}{2}\left[(\Omega_\kappa + \omega_\kappa) - \sqrt{(\Omega_\kappa - \omega_\kappa)^2 + 4g_\kappa^2} \right] \approx \pm\sqrt{\omega_1^2}$$

$$\omega_{2\pm} = \pm\frac{1}{2}\left[(\Omega_\kappa + \omega_\kappa) + \sqrt{(\Omega_\kappa - \omega_\kappa)^2 + 4g_\kappa^2} \right] \approx \pm\sqrt{\omega_2^2}$$

These approximated static band structures are drawn in Fig. 1C.

Bloch-Floquet band structures of the TVTL

For the calculation of Bloch-Floquet band structures, we first assumed that the resonator capacitance is periodically driven as $C_r(t) = C_c/[1 + \delta(t)]$ with a temporal periodicity of $2\pi/\Omega$; this assumption makes the Hamiltonian time periodic, i.e., $H_\kappa(t + 2\pi/\Omega) = H_\kappa(t)$. The temporal periodicity allows us to use the Fourier series expansion of the Hamiltonian, $H_\kappa(t) = \sum_q \exp(-jq\Omega t) H_\kappa^q$, and choose the solution of the Floquet form $\psi_\kappa(t) = \exp(-j\omega t) \sum_q \exp(-jq\Omega t) \psi_\kappa^q$. Consequently, the Hamilton's equations can be rearranged into a set of time-independent equations using the orthogonality of harmonic terms. The equations can be recast into an eigenvalue

problem with the following time-independent effective Floquet Hamiltonian matrix

$$\widetilde{H}_{\kappa}^{F} = \begin{bmatrix} \ddots & & & \\ & \widetilde{H}_{\kappa}^{0} + \Omega \mathrm{I} & \widetilde{H}_{\kappa}^{-1} & \widetilde{H}_{\kappa}^{-2} \\ & \widetilde{H}_{\kappa}^{+1} & \widetilde{H}_{\kappa}^{0} & \widetilde{H}_{\kappa}^{-1} \\ & \widetilde{H}_{\kappa}^{+2} & \widetilde{H}_{\kappa}^{+1} & \widetilde{H}_{\kappa}^{0} - \Omega \mathrm{I} \\ & & & \ddots \end{bmatrix}$$

The size of the Floquet Hamiltonian matrix depends on the harmonic order considered in the analysis and determines the number of shifted replicas of static bands appearing in the band structure. In the case where $\delta(t)$ is sinusoidal, i.e., $\delta(t) = \delta_0 \cos(\Omega t + \varphi_0)$, we can truncate the Floquet Hamiltonian matrix up to the first harmonic order without significant loss of accuracy. The calculated Bloch-Floquet band structures are shown in Fig. 1D and overlaid on the experimentally measured band structure in Fig. 2.

The Materials and Methods section should provide sufficient information to allow replication of the results. Begin with a section titled Experimental Design describing the objectives and design of the study as well as prespecified components.

Reduced Floquet Hamiltonian

The opening of a gap along the momentum axis is attributed to the nonreciprocal coupling between two dominant bands participating in the interaction, one of which is the static band and the other is the sideband. Therefore, the formation of dressed bands due to the driving-induced interaction between those two bands can be intuitively understood by constructing a 2×2 effective Hamiltonian matrix, the so-called reduced Floquet Hamiltonian. With the rotating-wave approximation followed by a basis transformation, the static component of the Floquet Hamiltonian can be diagonalized: $\overline{H}_{\kappa}^{0} = P^{-1}\widetilde{H}_{\kappa}^{0}P = \mathrm{diag}(\omega_{i\pm})$. Then, the reduced Floquet Hamiltonian is obtained by choosing only four elements from the entire Floquet Hamiltonian considering the driving-induced interaction between the involved bands. For the lossless case, the nonreciprocal coupling coefficients for the first-order sideband of the μth band and the static νth band are found to be

$$\kappa_{\mu\nu}^{F} = \frac{\Delta_{\nu}}{\Delta_{2}^{*} - \Delta_{1}^{*}} \frac{\omega_{\kappa}\delta_{0}}{4} e^{j\varphi_{M}}$$

where $\Delta_{\mu(\nu)} \equiv \Omega_{\kappa} - \omega_{\mu+(\nu+)}$. The reduced Bloch-Floquet band structures calculated from the reduced Floquet Hamiltonian are used for the non-Hermitian physics-based analyses in the main manuscript.

Inclusion of dissipative loss in resonators

The resonator dissipative loss can be considered by introducing the Rayleigh dissipation function and adding the corresponding nonconservative force into the equation of motion. A serially connected resistor is included in each constituting *LC* resonator as a source of dissipation. Then, the Rayleigh dissipation function in momentum space is found to be

$$\mathcal{F}_{\kappa} = \frac{1}{2}R|\dot{Q}_{\kappa}^{b}|^{2} = \gamma_{\kappa}\omega_{\kappa}(b_{\kappa}^{\dagger} - b_{-\kappa})(b_{-\kappa}^{\dagger} - b_{\kappa})$$

where γ_{κ} is the loss rate proportional to the resistance. By including the dissipative loss, the frequency of the static band becomes intrinsically complex valued as follows:

$$\omega_{1+} = \frac{1}{2}\left[(\Omega_{\kappa} + \omega_{\kappa} - j\gamma_{\kappa}) - \sqrt{(\Omega_{\kappa} - \omega_{\kappa} + j\gamma_{\kappa})^{2} + 4g_{\kappa}^{2}}\right] = -\omega_{1-}^{*}$$

$$\omega_{2+} = \frac{1}{2}\left[(\Omega_{\kappa} + \omega_{\kappa} - j\gamma_{\kappa}) + \sqrt{(\Omega_{\kappa} - \omega_{\kappa} + j\gamma_{\kappa})^{2} + 4g_{\kappa}^{2}}\right] = -\omega_{2-}^{*}$$

The band structures considering the dissipative loss were used to interpret the phase retardation measurements and non-Bloch band structures shown in Figs. 4 and 5.

Fabrication of samples and preparation of the measurement setup

The split-ring resonators comprising the photonic Floquet medium were patterned on low-loss dielectric substrates (RO4350B 30MIL, Rogers) by a printed circuit board manufacturing process. Then, a varactor diode (SMV-1247, Skyworks) was soldered to the resonator split gap and connected via an SMA (Sub-Miniature A) connector to external driving circuitry for periodic capacitance modulation (see Fig. 2B for the design of unit cells and their operation). The driving signal was generated and amplified by a signal generator (E4438C, Keysight) and a radio frequency amplifier (RUM43020-10, RFHIC), while its power was monitored before distributing the signal to the constituting unit cells. Each resonator was DC-biased using a bias tee (ZX85-40 W-63-S+, Mini-Circuits), and the operating DC bias voltage was optimized to ensure the large opening of a primary momentum gap. For spatiotemporal electric field probe scanning measurements, a rectangular waveguide with a DC servo-controlled movable upper plate was custom-made, and a quarter-wave monopole antenna was attached to the movable upper plate. In addition, a commercially available waveguide was used for the phase retardation and parametric oscillation measurements. Both waveguides have the same dimensions as the standard WR430 rectangular waveguide, whose recommended operation band ranges from 1.72 to 2.60 GHz. Schematics of the experimental setups are depicted in fig. S8.

Bloch-Floquet band structure construction by spatiotemporal field probing

The number of unit cells used to probe the Bloch-Floquet band structure was set to 36 to ensure maximal momentum space resolution under realistic driving conditions. In all the measurements, the distance between the nearest-neighbor unit cells was fixed to 10 mm. To provide a seeding field for spatiotemporal modal evolution inside the Floquet medium, an on-off keying signal (N5171B, Keysight) with a variable (angular) carrier frequency (ω) was fed into the input port of the waveguide (see fig. S8). To synchronize the acquisition at different spatial probe positions, a rising signal edge was used to trigger the whole measurement sequence. Experimental data were monitored with a spectrum analyzer (E4404B, Keysight) and a digital oscilloscope (DPO70804, Tektronix). To obtain high resolution along the frequency axis, the input frequency was scanned in 10-MHz steps. Then, the acquired spatiotemporal field was Fourier-transformed to reconstruct the Bloch-Floquet band structures. For clear visualization of static bands and Floquet sidebands, we mainly used three spatially resolved spectral components (ω, Ω − ω and Ω/2), and the Bloch-Floquet band was reconstructed by merging each spectral component with normalized amplitude on the frequency axis.

Non-Bloch band construction by phase retardation measurement

For characterization of phase retardation and construction of non-Bloch band structures, three measurements were sequentially

performed (see fig. S8). First, the phase retardation through an empty waveguide and a static resonator-loaded waveguide was measured as a function of frequency. Here, the measurement on the empty waveguide was used to subtract the phase retardation accumulated along the path outside the Floquet medium (i.e., the path from the source to the medium and the medium to a detector). We first checked the validity of this measurement scheme by reconstructing the static band structure and comparing it with the theoretically calculated structure. With driving on, the same measurement gives the non-Bloch band structures shown in the main manuscript (Fig. 5). For clear visualization of the driving-induced sidebands of negative frequency states, we mirror-imaged the measured curves with respect to the momentum gap frequency.

SUPPLEMENTARY MATERIALS

Supplementary material for this article is available at https://science.org/doi/10.1126/sciadv.abo6220

REFERENCES AND NOTES

1. D. N. Basov, R. D. Averitt, D. Hsieh, Towards properties on demand in quantum materials. *Nat. Mater.* **16**, 1077–1088 (2017).
2. T. Oka, S. Kitamura, Floquet engineering of quantum materials. *Annu. Rev. Condens. Matter Phys.* **10**, 387–408 (2019).
3. D. V. Else, C. Monroe, C. Nayak, N. Y. Yao, Discrete time crystals. *Annu. Rev. Condens. Matter Phys.* **11**, 467–499 (2020).
4. J. Zhang, P. W. Hess, A. Kyprianidis, P. Becker, A. Lee, J. Smith, G. Pagano, I.-D. Potirniche, A. C. Potter, A. Vishwanath, N. Y. Yao, C. Monroe, Observation of a discrete time crystal. *Nature* **543**, 217–220 (2017).
5. S. Choi, J. Choi, R. Landig, G. Kucsko, H. Zhou, J. Isoya, F. Jelezko, S. Onoda, H. Sumiya, V. Khemani, C. von Keyserlingk, N. Y. Yao, E. Demler, M. D. Lukin, Observation of discrete time-crystalline order in a disordered dipolar many-body system. *Nature* **543**, 221–225 (2017).
6. T. Oka, H. Aoki, Photovoltaic Hall effect in graphene. *Phys. Rev. B* **79**, 081406 (2009).
7. N. H. Lindner, G. Refael, V. Galitski, Floquet topological insulator in semiconductor quantum wells. *Nat. Phys.* **7**, 490–495 (2011).
8. K. Wintersperger, C. Braun, F. N. Ünal, A. Eckardt, M. Di Liberto, N. Goldman, I. Bloch, M. Aidelsburger, Realization of an anomalous Floquet topological system with ultracold atoms. *Nat. Phys.* **16**, 1058–1063 (2020).
9. M. C. Rechtsman, J. M. Zeuner, Y. Plotnik, Y. Lumer, D. Podolsky, F. Dreisow, S. Nolte, M. Segev, A. Szameit, Photonic Floquet topological insulators. *Nature* **496**, 196–200 (2013).
10. L. J. Maczewsky, J. M. Zeuner, S. Nolte, A. Szameit, Observation of photonic anomalous Floquet topological insulators. *Nat. Commun.* **8**, 13756 (2017).
11. L. He, Z. Addison, J. Jin, E. J. Mele, S. G. Johnson, B. Zhen, Floquet Chern insulators of light. *Nat. Commun.* **10**, 4194 (2019).
12. R. Fleury, A. B. Khanikaev, A. Alù, Floquet topological insulators for sound. *Nat. Commun.* **7**, 11744 (2016).
13. H. Chen, L. Y. Yao, H. Nassar, G. L. Huang, Mechanical quantum Hall effect in time-modulated elastic materials. *Phys. Rev. Appl.* **11**, 044029 (2019).
14. Y. Xia, E. Riva, M. I. N. Rosa, G. Cazzulani, A. Erturk, F. Braghin, M. Ruzzene, Experimental observation of temporal pumping in electromechanical waveguides. *Phys. Rev. Lett.* **126**, 095501 (2021).
15. N. Y. Yao, C. Nayak, L. Balents, M. P. Zaletel, Classical discrete time crystals. *Nat. Phys.* **16**, 438–447 (2020).
16. M. Fruchart, R. Hanai, P. B. Littlewood, V. Vitelli, Non-reciprocal phase transitions. *Nature* **592**, 363–369 (2021).
17. T. Ozawa, H. M. Price, N. Goldman, O. Zilberberg, I. Carusotto, Synthetic dimensions in integrated photonics: From optical isolation to four-dimensional quantum Hall physics. *Phys. Rev. A* **93**, 043827 (2016).
18. L. Yuan, Q. Lin, M. Xiao, S. Fan, Synthetic dimension in photonics. *Optica* **5**, 1396 (2018).
19. K. Lee, J. Son, J. Park, B. Kang, W. Jeon, F. Rotermund, B. Min, Linear frequency conversion via sudden merging of meta-atoms in time-variant metasurfaces. *Nat. Photonics* **12**, 765–773 (2018).
20. A. M. Shaltout, V. M. Shalaev, M. L. Brongersma, Spatiotemporal light control with active metasurfaces. *Science* **364**, eaat3100 (2019).
21. Y. Zhou, M. Z. Alam, M. Karimi, J. Upham, O. Reshef, C. Liu, A. E. Willner, R. W. Boyd, Broadband frequency translation through time refraction in an epsilon-near-zero material. *Nat. Commun.* **11**, 2180 (2020).
22. S. Mukherjee, M. C. Rechtsman, Observation of Floquet solitons in a topological bandgap. *Science* **368**, 856–859 (2020).
23. D. L. Sounas, A. Alù, Non-reciprocal photonics based on time modulation. *Nat. Photonics* **11**, 774–783 (2017).
24. K. Wang, A. Dutt, K. Y. Yang, C. C. Wojcik, J. Vučković, S. Fan, Generating arbitrary topological windings of a non-Hermitian band. *Science* **371**, 1240–1245 (2021).
25. K. Wang, A. Dutt, C. C. Wojcik, S. Fan, Topological complex-energy braiding of non-Hermitian bands. *Nature* **598**, 59–64 (2021).
26. Y. H. Wang, H. Steinberg, P. Jarillo-Herrero, N. Gedik, Observation of Floquet-Bloch states on the surface of a topological insulator. *Science* **342**, 453–457 (2013).
27. J. S. Martínez-Romero, O. M. Becerra-Fuentes, P. Halevi, Temporal photonic crystals with modulations of both permittivity and permeability. *Phys. Rev. A* **93**, 063813 (2016).
28. N. Chamanara, Z. L. Deck-Léger, C. Caloz, D. Kalluri, Unusual electromagnetic modes in space-time-modulated dispersion-engineered media. *Phys. Rev. A* **97**, 063829 (2018).
29. N. Wang, Z. Q. Zhang, C. T. Chan, Photonic Floquet media with a complex time-periodic permittivity. *Phys. Rev. B* **98**, 085142 (2018).
30. E. Riva, J. Marconi, G. Cazzulani, F. Braghin, Generalized plane wave expansion method for non-reciprocal discretely modulated waveguides. *J. Sound Vib.* **449**, 172–181 (2019).
31. S. Lee, J. Park, H. Cho, Y. Wang, B. Kim, C. Daraio, B. Min, Parametric oscillation of electromagnetic waves in momentum band gaps of a spatiotemporal crystal. *Photonics Res.* **9**, 142 (2021).
32. E. Lustig, Y. Sharabi, M. Segev, Topological aspects of photonic time crystals. *Optica* **5**, 1390–1395 (2018).
33. J. Park, B. Min, Spatiotemporal plane wave expansion method for arbitrary space–time periodic photonic media. *Opt. Lett.* **46**, 484–487 (2021).
34. F. Zhang, Y. Feng, X. Chen, L. Ge, W. Wan, Synthetic anti-PT Symmetry in a single microcavity. *Phys. Rev. Lett.* **124**, 053901 (2020).
35. A. Bergman, R. Duggan, K. Sharma, M. Tur, A. Zadok, A. Alù, Observation of anti-parity-time-symmetry, phase transitions and exceptional points in an optical fibre. *Nat. Commun.* **12**, 486 (2021).
36. H. Kazemi, M. Y. Nada, T. Mealy, A. F. Abdelshafy, F. Capolino, Exceptional points of degeneracy induced by linear time-periodic variation. *Phys. Rev. Appl.* **11**, 014007 (2019).
37. K. Rouhi, H. Kazemi, A. Figotin, F. Capolino, Exceptional points of degeneracy directly induced by space-time modulation of a single transmission line. *IEEE Antennas Wirel. Propag. Lett.* **19**, 1906–1910 (2020).
38. T. T. Koutserimpas, R. Fleury, Electromagnetic fields in a time-varying medium: Exceptional points and operator symmetries. *IEEE Trans. Antennas Propag.* **68**, 6717–6724 (2020).
39. J. R. Reyes-Ayona, P. Halevi, Observation of genuine wave vector (k or β) gap in a dynamic transmission line and temporal photonic crystals. *Appl. Phys. Lett.* **107**, 074101 (2015).
40. K. Yokomizo, S. Murakami, Non-Bloch band theory of non-Hermitian systems. *Phys. Rev. Lett.* **123**, 66404 (2019).
41. K. Kawabata, N. Okuma, M. Sato, Non-Bloch band theory of non-Hermitian Hamiltonians in the symplectic class. *Phys. Rev. B.* **101**, 195147 (2020).
42. C. Scheibner, W. T. M. Irvine, V. Vitelli, Non-Hermitian band topology and skin modes in active elastic media. *Phys. Rev. Lett.* **125**, 118001 (2020).
43. K. Sone, Y. Ashida, T. Sagawa, Exceptional non-Hermitian topological edge mode and its application to active matter. *Nat. Commun.* **11**, 5745 (2020).
44. J. B. Pendry, E. Galiffi, P. A. Huidobro, Gain mechanism in time-dependent media. *Optica* **8**, 636–637 (2021).
45. A. Marandi, Z. Wang, K. Takata, R. L. Byer, Y. Yamamoto, Network of time-multiplexed optical parametric oscillators as a coherent Ising machine. *Nat. Photonics* **8**, 937–942 (2014).

Acknowledgments: We thank S. Yu, X. Piao, and J. Choi for helpful discussions. **Funding:** This work was supported by the National Research Foundation of Korea (NRF) through the government of Korea (NRF-2017R1A2B3012364) (to J.P., H.C., S.L., Kyungmin Lee, Kanghee Lee, and B.M.), the Center for Advanced Meta-Materials (CAMM) funded by the Korean government (MSIP) as Global Frontier Project (NRF-2014M3A6B3063709) (to J.P., H.C., S.L., Ky.L., Ka.L., and B.M.), the National Research Foundation of Korea (NRF) through the government of Korea (NRF-2020R1C1C1012138) (to S.L.), and the Center for Theoretical Physics of Complex Systems (PCS) funded by the Korean government (MSIP) as IBS Project (IBS-R024-D1) (to J.-W.R. and H.C.P.). **Author contributions:** Conceptualization: B.M. Methodology: H.C., S.L., Ky.L., Ka.L., and S.J. Investigation: J.P. Visualization: J.P. and H.C. Supervision: B.M. Writing—original draft: J.P. and B.M. Writing—review and editing: All authors. **Competing interests:** The authors declare that they have no competing interests. **Data and materials availability:** All data needed to evaluate the conclusions in the paper are present in the paper and/or the Supplementary Materials.

Submitted 17 February 2022
Accepted 22 August 2022
Published 7 October 2022
10.1126/sciadv.abo6220